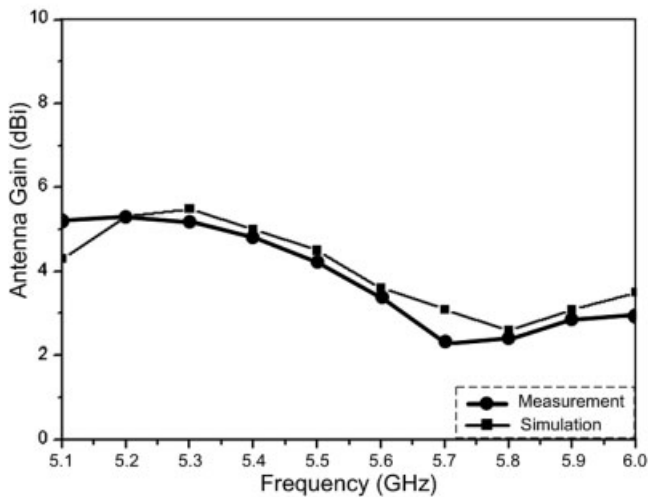


(a)



(b)

Figure 6 Measured and simulated antenna gain for the operating frequencies of (a) band I and (b) band II

maintain a front-to-end ratio of more than 10 dB in both the E-plane and H-plane. Meanwhile, the antenna gain versus frequency is also simulated and measured with two resonance bands, and the results are presented in Figure 6. As can be seen, compared with the simulations and measurements, the variations of antenna gain within the two bands are less than 0.9 dBi (band I) and 1.8 dBi (band II). In the measurements, gains of 3.6–5.0 dBi in band I and 2.4–5.3 dBi in band II are obtained, and a lower cross-polarization level of about -20 dB is achieved. In addition, the peak gain is 4.98 dBi at 3.1 GHz in band I and 5.3 dBi at 5.2 GHz in band II.

4. CONCLUSION

A novel dual-band antenna with modified quasi-Yagi planar structure has been presented in this paper. In practice, three shunt-connected dipoles of various lengths, which represent the reflector, resonator, and director, respectively, were etched in the ground plane. Meanwhile, a hook-shaped balun was proposed for the feed-line design. This antenna is characterized by unidirectional end-fire radiation patterns and dual-band impedance bandwidth. With the return loss is smaller than 10 dB, the dual bands cover the ranges 2.13–3.1 GHz and 5.15–5.9 GHz. Furthermore, gain vari-

ations of 3.6–5.0 dBi in band I and 2.4–5.3 dBi in band II are obtained. Both the measurement and simulation results of the return-loss responses and radiation patterns agree well.

The performance of the dual-band antenna includes wide bandwidth in each band, good radiation patterns in both principal planes, and a higher front-to-back pattern ratio. This antenna can be applied to the wireless-communication systems of IEEE 802.11a/b/g and Bluetooth.

REFERENCES

1. F.L. Bolzer and A. Louzir, Multiband annular slot antenna for WLAN applications, IEE 11th Int Conf Antennas Propagat, 2001, 529–532.
2. J.M. Ju, G.T. Jeong, J.H. Yoon, S.W. Ko, and K.S. Kwak, Design of multiple U-shaped slot microstrip patch antenna for 5-GHz band WLANs, Microwave Opt Technol Lett 43 (2004), 486–488.
3. T.Y. Wu, S.T. Fang, and K.L. Wong, A printed diversity dual-band monopole antenna for WLAN operation in the 2.4- and 5.2-GHz bands, Microwave Opt Technol Lett 36 (2003), 436–439.
4. C.J. Wang and W.T. Tsai, A stair-shaped slot antenna for the triple-band WLAN applications, Microwave Opt Technol Lett 39 (2003), 370–372.
5. J.W. Wu, H.M. Hsiao, J.H. Lu, and S.H. Chang, Dual-broadband design of rectangular slot antenna for 2.4- and 5-GHz wireless communication, Electron Lett 40 (2004), 1461–1463.
6. J. Huang and A.C. Densmore, Microstrip Yagi array antenna for mobile satellite vehicle application, IEEE Trans Antennas Propagat 39 (1991), 1024–1030.
7. W.R. Deal, N. Kaneda, J. Sor, Y. Qian, and T. Itoh, A new quasi-Yagi antenna for planar active antenna arrays, IEEE Trans Microwave Theory Tech 48 (2000), 910–918.
8. N. Kaneda, W.R. Deal, Q. Yongxi, R. Waterhouse, and T. Itoh, A broadband planar quasi-Yagi antenna, IEEE Trans Antennas Propagat 50 (2002), 1158–1160.
9. P.R. Grajek, B. Schoenlinner, and G.M. Rebeiz, A 24-GHz high-gain Yagu-Uda antenna array, IEEE Trans Antennas Propagat 52 (2004), 1257–1261.

© 2005 Wiley Periodicals, Inc.

TRANSMISSION AND SCATTERING ON INTERCONNECTS WITH VIA STRUCTURES

Chung-Chi Huang,¹ Kin Lun Lai,² Leung Tsang,^{1,2} Xiaoxiang Gu,¹ and Chong-Jin Ong¹

¹ Electrical Engineering Department
University of Washington
Box 352500

Seattle, WA 98195-2500

² Wireless Communications Research Center
City University of Hong Kong
Hong Kong SAR

Received 18 February 2005

ABSTRACT: Multiview interconnect structures for printed circuit boards (PCBs) have been analyzed by decomposing the geometry into exterior and interior structures. In this paper, we include the effects of dielectric substrates in the exterior structure. The exterior problem is solved by using the method of moments (MoM). The impedance-matrix elements are evaluated by using a fast method of calculating the layered-medium Green's function. The RWG basis functions are also utilized. Combined with the Foldy-Lax equation for solving the interior structure of a cylindrical vias problem, we analyze the transmission and scattering characteristics of interconnects with via structures. The numerical results of the scattering matrix are obtained for various via structures with a through-hole via and a single-layered via. The results obtained using commercial modeling tools such as HFSS and IE3D are also compared.

Key words: interconnects; vias; trace; layered medium; Green's function; scattering matrix

I. INTRODUCTION

In modern digital printed circuit boards (PCBs), electronic devices continue to operate in increasing speed over a broad band of high frequencies as they are closely packed on an ever-increasing number of signal layers on the circuit boards. Since via structures are commonly used to provide good routing paths between different power planes at multiple locations, it is necessary to meet the EMI and radiated-emissions requirements [1]. Vias also create considerable voltage breakdown and signal-integrity problems, such as signal attenuation, unwanted coupling (crosstalk), and switching noise. Various models of via structures have been performed in the past. Via coupling effects have been analyzed by means of equivalent magnetic frill-array models [2]. The effects of the via-hole structure were examined by thin-wire approximation and the matrix pencil method [3]. In our recent papers [4–7], we used the equivalence principle to decompose the interconnect problem into interior and exterior problems. The interior problem is solved using the dyadic magnetic-field Green's function based on cylindrical-wave expansions. The multiple interactions of vias are evaluated using the Foldy–Lax scattering formula. In these past papers, the exterior problem was simplified by using free-space Green's functions, without the consideration of dielectric substrates. In this paper, we address the practical layout for the exterior problem of via structures, where dielectric substrates are present between the traces and the reference ground plane. Our formulation considers a layered medium with traces and pads above the dielectric substrate. The vertical sections of the bent via are embedded in the dielectric substrate. Combined with the Foldy–Lax equation for solving the interior structure of cylindrical vias problem, we analyze the transmission and scattering characteristics of interconnects with via structures. Green's functions for the exterior problem are calculated based on a method of fast-calculating Sommerfeld integrals for layered medium [8]. The RWG basis functions [9] are also used.

Section 2 of this paper summarizes the formulation of a complete circuit-board problem by decomposing the original problem into the interior problem described by the Foldy–Lax multiple-scattering equations and then further decomposing the exterior problem into wire-antenna and short-circuit problems. Section 3 describes the formulation of the exterior problem using integral equations, RWG basis functions, Galerkin's method, and impedance-matrix computation. We discuss the fast-calculation methods

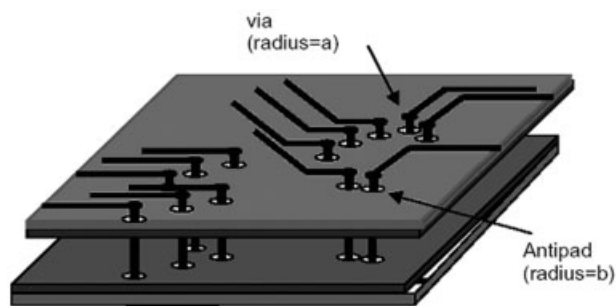


Figure 1 Typical layout of a printed circuit board

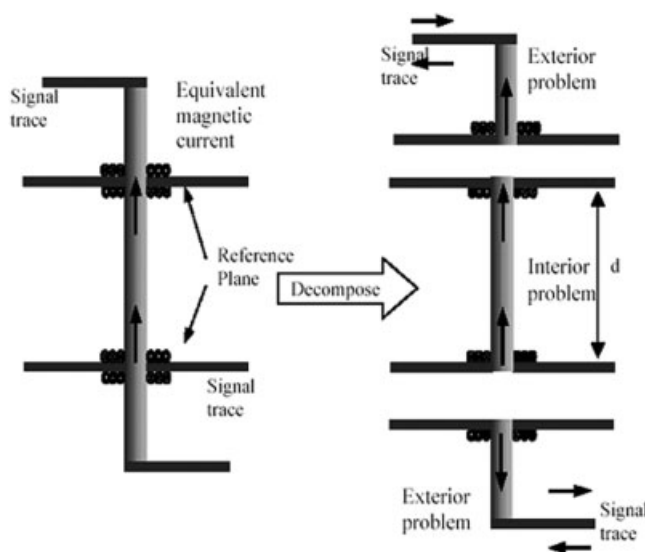


Figure 2 Decomposition of the original problem into exterior and interior problems

of the layered-medium dyadic Green's functions. In section 4, the numerical results are illustrated and interpreted for a wide frequency range up to 14 GHz. We consider vias with various exterior parameters, which includes pad radii, antipad radii, and layer thicknesses of the exterior and interior dielectric substrates. To verify the accuracy of the results, we compare our results with those obtained using HFSS and IE3D. The differential signaling of the common and differential modes of coupled interconnects are illustrated.

2. FORMULATION

Figure 1 shows the geometrical configuration of a printed circuit board. The traces are located on the dielectric substrates above the signal planes or reference ground planes and the cylindrical vias are passing through the planar waveguides. The microstrip structure is decomposed into interior and exterior problems, as shown in Figure 2, by using the equivalence principle. The equivalent magnetic surface currents are placed on the two sides of the via apertures with a PEC in-between. Then, the exterior and interior problems are solved separately. The solutions of the two separate problems are connected by imposing the continuity of the electrical currents and tangential magnetic fields as the boundary conditions.

2.1. Exterior Problem

The layout of the exterior structure consists of metal strips (signal traces), circular via pads, and the vertical section of a cylindrical via bent into the reference ground plane. Dielectric media are in-between the horizontal signal trace and the reference ground plane. We further decompose the exterior problem into the wire-antenna and short-circuit problems, as shown in Figure 3. On the surface of the metal strip, the pad, and the bent via, a set of electric-field integral equations (EFIEs) are formulated. After the current \vec{I} along the microstrip and bent via is solved in the integral equations, the matrix pencil method is applied to retrieve the traveling wave components \vec{A} and \vec{B} . For the short circuit problem, we use a delta gap source. The current at the short circuit end \vec{I}_{sc} and short-circuit reflection coefficient $\vec{\Gamma}_{sc}$ are then calculated. For the wire-antenna problem, the voltage source \vec{V} at the via aperture is the driving source for the antenna. The input admittance of the

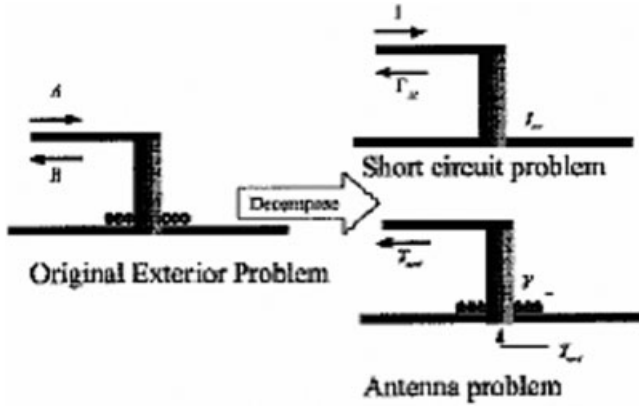


Figure 3 Decomposition of the exterior problem

wire antenna \bar{Y}_{ant} and the amplitude of the excited TEM mode in wire antenna \bar{T}_{ant} are calculated. A matrix equation is used to characterize the exterior structure as follows:

$$\begin{bmatrix} B \\ I_1 \end{bmatrix} = \begin{bmatrix} \Gamma_{sc} & T_{ant} \\ I_{sc} & Y_{ant} \end{bmatrix} \begin{bmatrix} A \\ V \end{bmatrix}. \quad (1)$$

When two traces are coupled with each other, Eq. (1) is extended to a 4×4 matrix as follows:

$$\begin{bmatrix} B_1 \\ I_1 \\ B_2 \\ I_2 \end{bmatrix} = \begin{bmatrix} \Gamma_{sc11} & T_{ant11} & \Gamma_{sc12} & T_{ant12} \\ I_{sc11} & Y_{ant11} & I_{sc12} & Y_{ant12} \\ \Gamma_{sc21} & T_{ant21} & \Gamma_{sc22} & T_{ant22} \\ I_{sc21} & Y_{ant21} & I_{sc22} & Y_{ant22} \end{bmatrix} \begin{bmatrix} A_1 \\ V_1 \\ A_2 \\ V_2 \end{bmatrix}, \quad (2)$$

where the subscripts in each parameter correspond to the trace index. The current at the two via apertures I_1 and I_2 are solved from integral equations and the four traveling-wave components, A_1 , B_1 , A_2 , and B_2 , are extracted by using the matrix pencil method. Then, all the 16 parameters in the 4×4 matrix in Eq. (2) can be solved by various conditions of the short-circuit and wire-antenna problems.

2.2. Interior Problem

For the interior problem, the Foldy-Lax equations have been adopted to solve for the full-wave solution. In the Foldy-Lax equation, the waveguide modes in cylindrical-wave expansions are utilized. A preconditioned sparse-matrix canonical-grid (SMCG) method [7] is used to solve the Foldy-Lax equations when there are large numbers of vias. After the matrix solutions are solved, the admittance matrix \bar{Y} of the interior problem is calculated by relating the port voltages and currents between the upper ports and the bottom ports, given by

$$\begin{bmatrix} \bar{I}^u \\ -\bar{I}^b \end{bmatrix} = -\bar{Y} \begin{bmatrix} -\bar{V}^u \\ \bar{V}^b \end{bmatrix}, \quad (3)$$

where \bar{Y} is a $2N_{int} \times 2N_{int}$ matrix, and N_{int} is the number of vias for the interior problem. The admittance matrix can be expressed as

$$\bar{Y} = \begin{bmatrix} \bar{Y}^{uu} & -\bar{Y}^{ub} \\ -\bar{Y}^{bu} & \bar{Y}^{bb} \end{bmatrix}. \quad (4)$$

Due to the reflection symmetry, we also have $\bar{Y}^{ub} = \bar{Y}^{bu}$ and $\bar{Y}^{uu} = \bar{Y}^{bb}$.

2.3. Combination of the Exterior and Interior Problems

The solutions of the exterior and interior problems separately lead to respective microwave-circuit network representations. To calculate the transmission and scattering of the complete problem, we relate the admittance matrix \bar{Y} found in the interior- and exterior-problem parameters, $\bar{\Gamma}_{sc}$, \bar{T}_{ant} , \bar{I}_{sc} , and \bar{Y}_{ant} . The combined problem of the interior and exterior problems gives rise to the $2N \times 2N$ scattering matrix \bar{S} , where N is the number of vias:

$$\bar{S} = \begin{bmatrix} \bar{\Gamma}_{sc}^u & \bar{0}_N \\ \bar{0}_N & \bar{\Gamma}_{sc}^b \end{bmatrix} + \begin{bmatrix} -\bar{T}_{ant}^u & \bar{0}_N \\ \bar{0}_N & \bar{T}_{ant}^b \end{bmatrix} \times \begin{bmatrix} \bar{Y}^{uu} + \bar{Y}_{ant}^u & \bar{Y}^{ub} \\ -\bar{Y}^{bu} & -\bar{Y}^{bb} - \bar{Y}_{ant}^b \end{bmatrix}^{-1} \begin{bmatrix} \bar{\Gamma}_{sc}^u & \bar{0}_N \\ \bar{0}_N & \bar{\Gamma}_{sc}^b \end{bmatrix} \quad (5)$$

In (5), the superscripts u and b from the exterior-problem parameters represent the values of the upper and bottom ports, respectively. For a multilayer PCB, the solutions can also be cascaded layer-by-layer in order to obtain the final solution.

3. INTEGRAL EQUATIONS FOR EXTERIOR PROBLEM

In the exterior problem (Fig. 3), we need to calculate $\bar{\Gamma}_{sc}$, \bar{T}_{ant} , \bar{I}_{sc} , and \bar{Y}_{ant} . The exterior structure is decomposed into wire-antenna and short-circuit problems.

3.1. Short-Circuit Problem

First, we consider the short-circuit problem (Fig. 3), with $V = 0$ in Eq. (1). Then, the TEM wave amplitude B and the current I_1 for a single trace with bent via are expressed as

$$B = \Gamma_{sc} A, \quad (6)$$

$$I_1 = I_{sc} A. \quad (7)$$

The unknown current distribution \bar{J}_s and the charge distribution ρ_s are induced on the microstrip and the via. They are governed by the following mixed-potential integral equation (MPIE):

$$\hat{n} \times \left[j\omega \int_s \bar{G}_{11}^A(\bar{r}, \bar{r}') \cdot \bar{J}_s(\bar{r}') ds' + \nabla_s \int_s G_{11}^V(\bar{r}, \bar{r}') \rho_s(\bar{r}') ds' \right] = \hat{n} \times \bar{E}^{inc}(\bar{r}), \quad (8)$$

where the \bar{G}_{11}^A and G_{11}^V are the Green's function for the vector and scalar potentials, respectively. With regard to the two indices in the subscript, the first index refers to the observation region and the second index refers to the region of the source point. Region 1 is the dielectric substrate and region 0 is the air above. In the following subsections, we describe efficient ways of computing \bar{G}_{11}^A and G_{11}^V , and the impedance-matrix elements. In the short-circuit problem, a gap-source in an infinitesimal small gap is introduced as the incident field on the right-hand side of Eq. (8). After solving for the unknown current I_1 in Eq. (7), we use the matrix pencil method to extract A and B . In our exterior formulation, we are only interested in the reflection on the trace compared with the incident amplitude. The open-end discontinuity at the source part will not affect the ratio of B/A . Also, the short-circuit current is calculated. By relating A , B , and I_1 in Eqs. (6) and (7), Γ_{sc} and I_{sc} can be obtained.

3.1.1. Dyadic Green's Function For Vector and Scalar Potentials. The vector potential Green's function \bar{G}_{11}^A has three components:

$$\bar{G}_{11}^A = (\hat{x}\hat{x} + \hat{y}\hat{y})G_{11xx}^A + (\hat{z}\hat{x} + \hat{z}\hat{y})G_{11zx}^A + \hat{z}\hat{z}G_{11zz}^A$$

$$= \begin{bmatrix} G_{11xx}^A & 0 & 0 \\ 0 & G_{11xx}^A & 0 \\ G_{11zx}^A & G_{11zx}^A & G_{11zz}^A \end{bmatrix}, \quad (9)$$

where the source and observation points are located in region 1. The scalar-potential Green's function differs between the horizontal electric dipole (HED) and the vertical electric dipole (VED):

$$G_{11}^V = \begin{cases} G_{11x}^V = G_{11y}^V & \text{for HED} \\ G_{11z}^V & \text{for VED} \end{cases}. \quad (10)$$

The Sommerfeld integral representations of the Green's functions are given in [10].

3.1.2. Fast-Calculating Approach of Sommerfeld Integrals Applied in Layered-Medium Green's Functions. Two complementary methods are used [8] to evaluate the Sommerfeld integrals of \bar{G}_{11}^A , G_{11}^V , and \bar{G}_{11}^{EM} . The dyadic Green's function is \bar{G}_{11}^{EM} (as described in a subsequent section). For interconnect problems in printed circuit boards, the frequencies usually range from 500 MHz to 20 GHz, whereas the distances range from 0.01 to 10 free-space wavelengths. There are also varying dielectric thicknesses. A fast and robust method is needed to evaluate the layered-medium Green's functions with the following requirements: (i) multi-layered medium, (ii) lossless and lossy dielectrics, (iii) a wide range of frequencies corresponding to a wide range of thicknesses, and (iv) a wide range of distances ρ , ranging from 0.01 to 10 free-space wavelengths. To cover these wide ranges of variations, and to satisfy all these requirements, we use two complementary methods to calculate the layered-medium Green's functions. The first method is to solve problems of moderate thickness of d (total thickness), with $d > 0.05\lambda_0$. It calculates the Green's functions using fast Fourier transform (FFT) based on the half-space extraction method. The computation time for simultaneously evaluating the Green's functions of 200 different source-to-field distances ranging from 0.01 to 10 free-space wavelengths for each frequency is about 20 s. The second method is applied for total thickness with $0 < d \leq 0.05\lambda_0$. It uses the numerical integration along the vertical branch cut and combine that with the surface-wave pole extraction. The time of calculating 200 different ρ , ranging from 0.01 to 10 free-space wavelengths, is about 30 s for each frequency. The surface-wave poles are extracted by means of the Newton-Raphson method, which can be easily implemented for multilayered media. There are no contributions from the leaky-wave poles for d less than 0.05 wavelengths when the vertical branch cut is chosen as the path of integration. Furthermore, the components of the Green's function are precalculated and a 3D interpolation lookup table is constructed.

3.1.3. Meshing the Exterior Structure with RWG Basis Functions. The unknown surface current in Eq. (8) on the trace and bent via is meshed by RWG basis functions, as shown in Figure 4. Usually the height of the vertical section of the exterior structure d_1 is small, and one rectangular cell (or two triangular cells) will be enough. The circular pad is approximated by a polygon. The choice of the number of sides of the polygon depends on the required accuracy. The vertical cylindrical section is also approximated by polygonal structures, which can be either hexagons or rectangles. Usually, the choice of rectangle is sufficiently accurate for the vertical-via section. The surface-current density using RWG basis functions can be written as a linear combination of a set of basis functions with unknown coefficients I_n as follows:

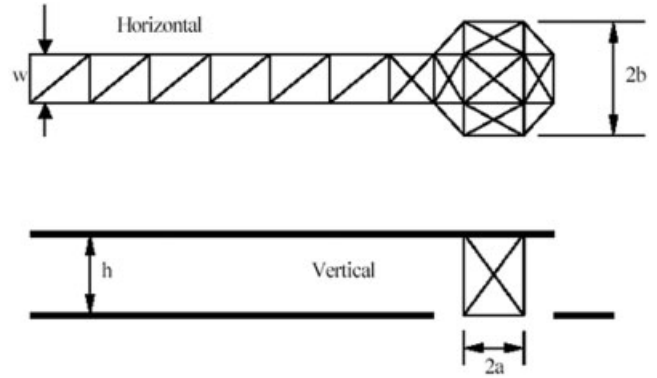


Figure 4 Meshing of the junction using RWG basis functions

$$\bar{J}_s^h(\vec{r}) = \sum_{n=1}^{N_1} I_n^h \bar{f}_n^h(\vec{r}), \quad (11)$$

$$\bar{J}_s^v(\vec{r}) = \sum_{n=N_1+1}^{N_1+N_2} I_n^v \bar{f}_n^v(\vec{r}), \quad (12)$$

where N_1 is the number of the interior edges of the triangular patch, plus the junction edge connecting the triangular patch and rectangular patch, and N_2 is the number of horizontal edges of the rectangular patch including the junction edge. In Eqs. (11) and (12), \bar{f}_n^h and \bar{f}_n^v are the horizontal and vertical RWG basis functions, respectively. A full RWG basis function consists of the plus and minus cells that are assigned to each interior edge. Using Galerkin's testing and transferring the derivatives in Eq. (8), the integral equation is then converted into the following matrix equation:

$$\bar{Z}\bar{I} = \bar{b}. \quad (13)$$

In the short-circuit problem, the right-hand side of Eq. (13) assumes the form

$$\bar{b} = [1 \quad 0 \quad \dots \quad 0]^T, \quad (14)$$

where the unity is at the cell where the field source is. Furthermore, Eq. (13) can be written into the following form with horizontal and vertical current elements:

$$\begin{bmatrix} \bar{Z}_{hh} & \bar{Z}_{hv} \\ \bar{Z}_{vh} & \bar{Z}_{vv} \end{bmatrix} \begin{bmatrix} \bar{I}_h \\ \bar{I}_v \end{bmatrix} = \begin{bmatrix} \bar{b}_h \\ \bar{b}_v \end{bmatrix}, \quad (15)$$

where

$$\bar{Z}_{hh} = j\omega \langle \bar{f}_m^h, \bar{G}_{xx,yy}^A * \bar{f}_n^h \rangle - \frac{j}{\omega} \langle \nabla_s \cdot \bar{f}_m^h, G_{yy}^V * \nabla'_s \cdot \bar{f}_n^h \rangle \quad (16)$$

$$= j\omega \langle \bar{f}_{mx}^h, G_{xx}^A * \bar{f}_{nx}^h \rangle + j\omega \langle \bar{f}_{my}^h, G_{yy}^A * \bar{f}_{ny}^h \rangle - \frac{j}{\omega} \langle \nabla_s \cdot \bar{f}_m^h, G_x^V * \nabla'_s \cdot \bar{f}_n^h \rangle, \quad (17)$$

$$\bar{Z}_{hv} = -\frac{j}{\omega} \left\langle \nabla_s \cdot \bar{f}_m^h, G_z^V * \frac{\partial f_{nz}^v}{\partial z} \right\rangle, \quad (18)$$

$$\bar{Z}_{vh} = j\omega \langle \bar{f}_m^v, \bar{G}_{zx,xy}^A * \bar{f}_n^h \rangle - \frac{j}{\omega} \langle \nabla_s \cdot \bar{f}_m^v, G_z^V * \nabla'_s \cdot \bar{f}_n^h \rangle \quad (19)$$

$$= j\omega \langle \bar{f}_{mz}^v, G_{zx}^A * \bar{f}_{nx}^h \rangle + j\omega \langle \bar{f}_{mz}^v, G_{zy}^A * \bar{f}_{ny}^h \rangle - \frac{j}{\omega} \left\langle \frac{\partial \bar{f}_{mz}^v}{\partial z}, G_x^V * \nabla'_s \cdot \bar{f}_n^h \right\rangle, \quad (20)$$

$$\bar{Z}_{vv} = j\omega \langle \bar{f}_m^v, \bar{G}_{zz}^A * \bar{f}_n^v \rangle - \frac{j}{\omega} \langle \nabla'_s \cdot \bar{f}_m^v, G_z^V * \nabla'_s \cdot \bar{f}_n^v \rangle \quad (21)$$

$$= j\omega \langle \bar{f}_{mz}^v, G_{zz}^A * \bar{f}_{nz}^v \rangle - \frac{j}{\omega} \left\langle \frac{\partial \bar{f}_{mz}^v}{\partial z}, G_z^V * \frac{\partial \bar{f}_{nz}^v}{\partial z} \right\rangle. \quad (22)$$

In Eqs. (16)–(22), $\langle \cdot, \cdot \rangle$ and $*$ denote the inner product and the convolution, respectively. Also, $\bar{f}_n^h = f_{nx}^h \hat{x} + f_{ny}^h \hat{y}$ and $\bar{f}_n^v = f_{nz}^v \hat{z}$. For the RWG basis functions, the divergences of the basis and testing functions in Eqs. (16)–(22) are constant across the plus patch or minus patch. In Eqs. (15)–(22), \bar{Z}_{hh} represents the interactions between the horizontal triangular patches on the strip, \bar{Z}_{hv} and \bar{Z}_{vh} stand for the interactions between the rectangular patch on the vertical surface and the horizontal triangular patches on the strip, and \bar{Z}_{vv} relates to the interactions between two rectangular patches on the vertical surface. Evaluations of the self-patch interactions are required for \bar{Z}_{hh} and \bar{Z}_{vv} .

3.2. Wire-Antenna Problem

Next, we consider the wire-antenna problem. There is a magnetic-current source at the via aperture, which makes A nonzero. Using that in Eq. (1), the TEM wave amplitude B and the current I_1 can be expressed in terms of V and A as follows:

$$B = \Gamma_{sc} A + T_{ant} V, \quad (23)$$

$$I = I_{sc} A + Y_{ant} V, \quad (24)$$

where a unit voltage source, $V = 1$, is used. The unknown current distribution \bar{J}_s and the charge distribution ρ_s are induced on the microstrip and the via. The same mixed-potential integral equation (MPIE) is also formulated using Galerkin's testing and RWG basis functions. For this problem, because the geometry is the same as in the short-circuit problem, the impedance matrix is the same as in Eq. (13) while the right-hand side is different. In the wire-antenna problem, the voltage V gives rise to the magnetic-current source at the via aperture \bar{M}_s . The incident electric field \bar{E}^{inc} is next calculated by

$$\int_a \bar{G}_{11}^{EM}(\bar{r}, \bar{r}') \cdot \bar{M}_s(\bar{r}') ds = \bar{E}^{inc}(\bar{r}), \quad (25)$$

where the integration is carried over the area of the via aperture a . The dyadic Green's function, \bar{G}_{11}^{EM} is the electric-field layered-medium Green's function of magnetic-current source. The two fast complementary methods are also applied to evaluate \bar{G}_{11}^{EM} and the formulations are described in the following subsection. Furthermore, by applying the same RWG basis function and Galerkin's procedures, the integral equation in Eq. (25) is converted into the matrix equation, where the right-hand side of the equation is given by

$$b_n = \int_{s_n} ds \bar{f}_n(\bar{r}) \cdot \bar{E}^{inc}(\bar{r}). \quad (26)$$

After solving the unknown current coefficients I_1 at the via aperture, the matrix pencil method is applied again to retrieve A and B . Since I_{sc} and Γ_{sc} are solved in short circuit problem, T_{ant} and Y_{ant} can be extracted by Eqs. (23) and (24).

3.2.1. Electric-Field Layered-Medium Green's Function of Magnetic Current Source \bar{G}_{11}^{EM} .

Only six components are required for \bar{G}_{11}^{EM} due to the fact that the magnetic current \bar{M}_s only has \hat{x} and \hat{y} components in the wire-antenna problem:

$$\bar{G}_{11}^{EM} = G_{xx}^{EM} \hat{x} \hat{x} + G_{yx}^{EM} \hat{y} \hat{x} + G_{xy}^{EM} \hat{x} \hat{y} + G_{yy}^{EM} \hat{y} \hat{y} + G_{zy}^{EM} \hat{z} \hat{y}. \quad (27)$$

The components can be expressed in terms of three scalar functions as follows:

$$G_{xx}^{EM}(\rho, z, \phi) = -[U_\phi(\rho, z) + U_\rho(\rho, z)] \cos \phi \sin \phi, \quad (28)$$

$$G_{yx}^{EM}(\rho, z, \phi) = U_\rho(\rho, z) \cos^2 \phi - U_\phi(\rho, z) \sin^2 \phi, \quad (29)$$

$$G_{zx}^{EM}(\rho, z, \phi) = U_z(\rho, z) \sin \phi, \quad (30)$$

$$G_{yy}^{EM}(\rho, z, \phi) = [U_\phi(\rho, z) + U_\rho(\rho, z)] \cos \phi \sin \phi, \quad (31)$$

$$G_{xy}^{EM}(\rho, z, \phi) = -U_\rho(\rho, z) \sin^2 \phi + U_\phi(\rho, z) \cos^2 \phi, \quad (32)$$

$$G_{zy}^{EM}(\rho, z, \phi) = -U_z(\rho, z) \cos \phi, \quad (33)$$

where U_ρ , U_ϕ , and U_z are the three scalar functions given in [10].

4. NUMERICAL RESULTS AND DISCUSSION

In the numerical results presented in this section, both the exterior and interior structures have a single-layered dielectric substrate. Both substrates have relative permittivity ϵ_r equal to 4. In the simulations, a through-hole via and a single-layered via are used. The simulations are carried out on a personal computer with a 2.4-GHz CPU and 1-GB memory. The computational time for solving the scattering matrix is 3.2 min per frequency. In the process of calculating the impedance matrix elements, the computation for the layered-medium Green's function for MPIE takes less than 30 s per frequency for geometries of 200 different source-to-field distances.

4.1. A Through-Hole Via

We first consider various interconnect structures of various sizes with a through-hole vertical via. Figure 5 shows the scattering parameters for transmission and reflection of the via, with and without the consideration of interior-problem solutions, respectively. The via's inner radius a is 0.127 mm, the antipad radius b is 0.381 mm, the via pad radius r is 0.381 mm, and the width w of the strip is 0.381 mm. The length of the trace is 9.4 mm. The layer thickness h for the exterior-layer structure is 0.254 mm. As can be seen, the transmission loss is significant when the interior problem is not considered, especially for high frequencies. The results show that the effect of the interior structure is significant.

4.2. Comparison of the Simulation Results Using HFSS and IE3D

To verify the accuracy of our results, we compare them with the results of HFSS and IE3D, as shown in Figure 6. The simulation results show the propagation characteristics of the via structure with various via-hole parameters up to a frequency of 14 GHz. The varying parameters include the antipad radius b , the pad radius r , and the exterior-layer thickness h . The geometrical configurations

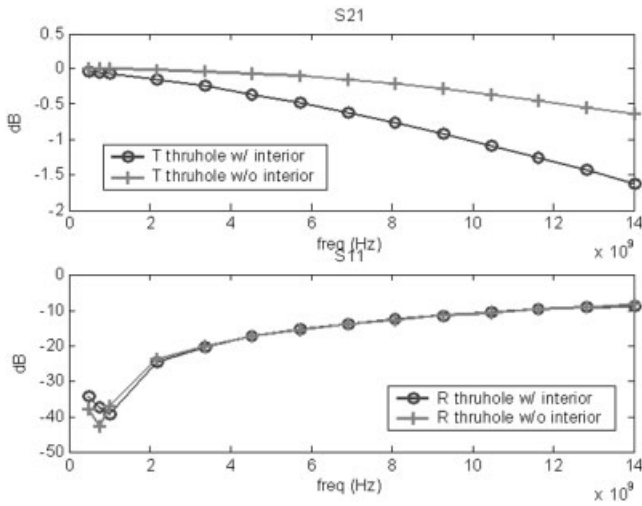


Figure 5 Transmission and reflection characteristics of a through-hole via with and without analysis of the interior problem

are the same as that in Figure 5 and the layer thickness d for the inner-layer structure is 0.508 mm. The execution of the HFSS ver. 9.1 simulation proceeds as follows. A radiation boundary condition is imposed on the boundary of an air box. The via structure is placed inside the air box. The length of the air box boundary is 18.5 mm, the width is 7.62 mm, and the total height of that boundary is about 15 times larger than the exterior-layer thickness, which is about 3.81 mm. We simulate by choosing 901 different frequencies up to 15 GHz with 2% error for the adaptive solutions of accurate field solutions. Figure 6 shows that the simulation results based on the methodology of this paper are generally in good agreement with those using HFSS. However, there are some oscillations in the HFSS results. The discrepancies with HFSS can be attributed to the differences in modeling between the two methods. Since HFSS uses the finite-element method (FEM) for the implementation, a boundary is needed to wrap the structure. The results using HFSS are obtained by means of an absorbing

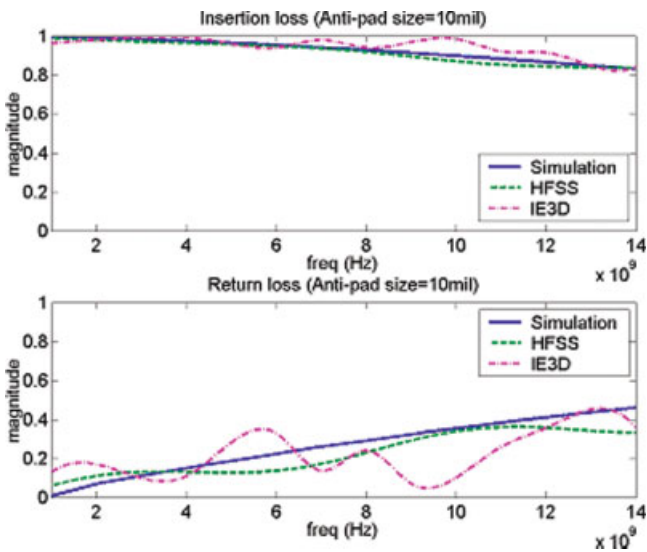


Figure 6 Comparison of the simulated insertion and return losses with those of HFSS and IE3D for a single-layered via (anti-pad radius is 10 mil). [Color figure can be viewed in the online issue, which is available at www.interscience.wiley.com.]

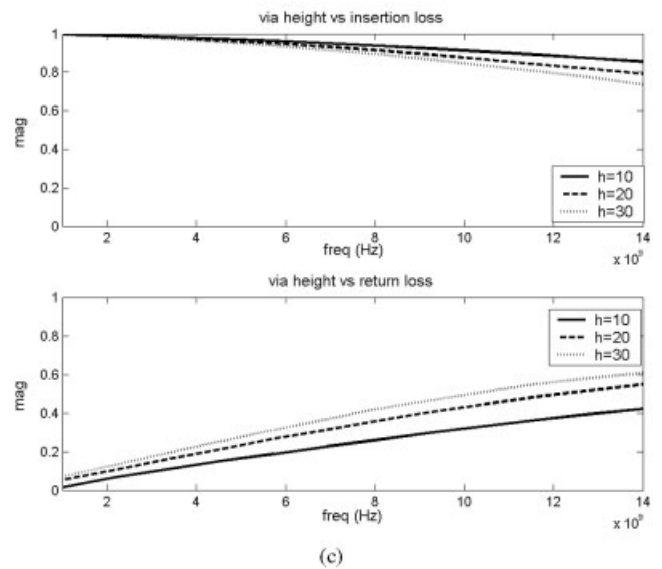
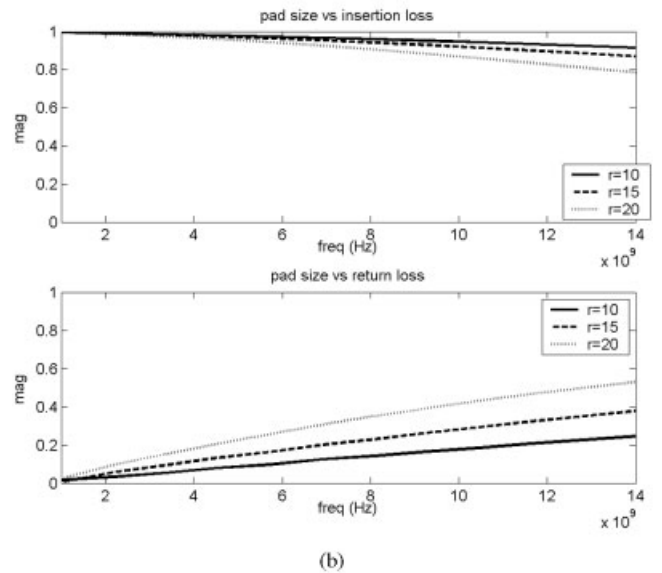
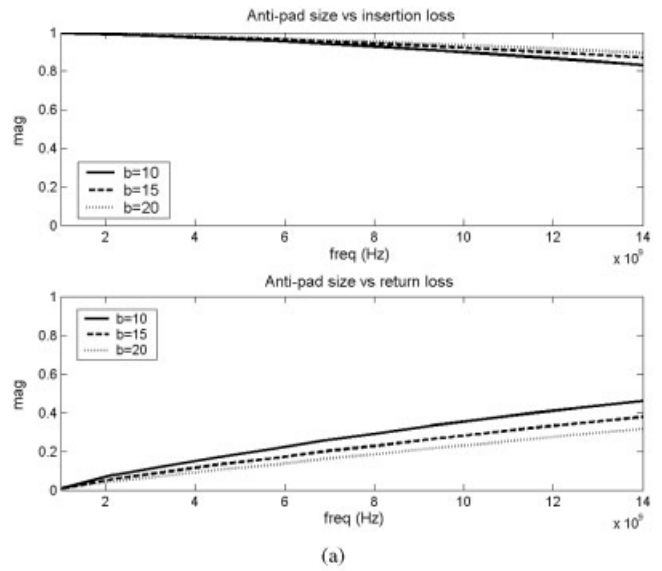


Figure 7 Transmission and reflection characteristics of a single-layered via for different (a) anti-pad radii and (b) pad radii (c) exterior layer thickness

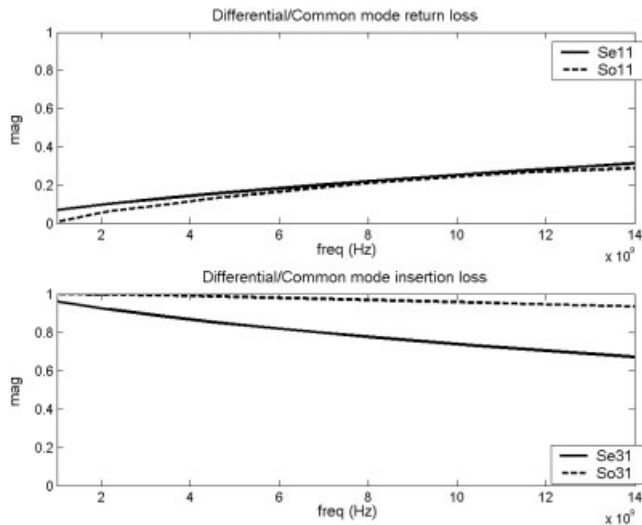


Figure 8 Transmission and reflection characteristics of differential signaling for the differential and common modes

boundary condition on a layered medium of finite extent. On the other hand, for the approach taken in this paper, the Green's function is derived for a layered medium of infinite extent. The absorbing boundary condition in HFSS is not perfectly absorbing, as there are reflections from the boundaries creating oscillations in the results. On the other hand, the results of IE3D are clearly erroneous.

4.3. A Through-Hole Via

We investigate the transmission and reflection behavior of a single-layered via with different via-hole parameters, such as antipad radius b , pad radius r , and exterior-substrate thickness h , from 1 to 15 GHz. The geometrical configurations are the same as before and the layer thickness d for the inner-layer structure is 0.508 mm. Figure 7 shows the transmission and reflection characteristics. In Figure 7(a), with the larger hole radius of the antipad, the insertion loss decreases and the return loss increases. The results show that the larger hole can maximize the voltage-breakdown spacing between the via and the reference ground plane [11]. The results shown in Figure 7(b) indicate that, by increasing the pad size of the via, the insertion loss decreases in a rapid manner while the reflection loss increases much more with increasing frequencies. The results show that a smaller pad can maintain a strong reference to the ground for single-ended signals and ground-referenced signals [11]. In Figure 7(c) by increasing the exterior-layer thickness, the losses become significant. To summarize, to obtain a better design of the via structures, the through-hole via needs to have a large antipad radius and a small pad radius, that is, small in both exterior- and interior-layer thickness.

We illustrate differential signaling by considering two interconnects with vertical vias in the common and differential modes. The via radius is 0.127 mm, the pad radius is 0.254 mm, the antipad radius is 0.381 mm, and the trace width is 0.381 mm. The exterior layer thickness is 0.102 mm. The air gap between the two traces is 0.381 mm. The exterior problem parameters \bar{I}_{sc} , \bar{T}_{ant} , \bar{I}_{sc} , and \bar{Y}_{ant} are solved by solving the exterior problem four times and using Eq. (2). Figure 8 shows the characteristics of return loss, insertion loss, and radiation loss with frequency. The cases with layer thicknesses 0, 0.762, and 1.524 mm are shown. In the figure, Se11 stands for even mode while So11 stands for the odd mode. It

is clear from the results that differential signaling reduces the insertion and return losses significantly.

5. CONCLUSION

In the full-wave electromagnetic analysis of vias and interconnect structures, the microstrip interconnect problem is divided into interior and exterior problems. The exterior problem is solved by the MoM and RWG basis functions with the rapid calculation of the layered-medium Green's function. The interior problem is solved by using Foldy-Lax equations. The simulation results are illustrated for a wide range of frequencies up to 14 GHz for analysis of via structures. Presently, we are extending the method to large problems in the exterior problem using fast matrix solvers.

ACKNOWLEDGMENTS

This work was partly supported by the Intel Corporation and the City University of Hong Kong Strategic Research Grant no. 7001550.

REFERENCES

1. J. Fang, J. Zhao, and J. Zhang, Shorting via arrays for the elimination of package resonance to reduce power supply noise in multilayered area-array IC package, IEEE Symp IC/Package Design Integration, 1998.
2. Q. Gu, A. Tassoudji, S.Y. Poh, R.T. Shin, and J.A. Kong, Coupled noise analysis for adjacent vias in multilayered digital circuits, IEEE Trans Circ Syst 41 (1994), 796–804.
3. S.G. Hsu and R.B. Wu, Full-wave characterization of a through hole via in multi-layered packaging, IEEE Trans Microwave Theory Tech 43 (1995), 1073–1081.
4. L. Tsang, H. Chen, C. Huang, and V. Jandhyala, Modeling of multiple scattering among vias in planar waveguide using foldy-lax equations, Microwave Opt Technol Lett 31 (2001), 201–208.
5. H.F. Chen, C.C. Huang, L. Tsang, and Q. Li, Analysis of via discontinuity, Microwave Opt Technol Lett 39 (2003), 290–295.
6. H. Chen, Q. Li, L. Tsang, C.C. Huang, and V. Jandhyala, Analysis of large number of vias and differential signaling in multi-layered structures, IEEE Trans Microwave Theory Tech (2003), 818–828.
7. C.C. Huang, L. Tsang, C.H. Chan, and K.H. Ding, Multiple scattering among vias in planar waveguides using preconditioned SMCG method, IEEE Trans Microwave Theory Tech 52 (2004), 20–28.
8. K.L. Lai, L. Tsang, and C.C. Huang, Spatial Domain Green's Functions for Planar Multi-layered Structures, Microwave Opt Tech Lett 44 (2005), 86–91.
9. D.R. Wilton, S.M. Rao, A.W. Glisson, D.H. Schaubert, O.M. Al-bundak, and C.M. Butler, Potential integrals for uniform and linear source distribution on polygonal and polyhedral domains, IEEE Trans Antennas Propagat 32 (1984), 276–281.
10. C.C. Huang, Full-wave modeling and characterization of high-frequency interconnect in layered medium, Ph.D. dissertation, University of Washington, 2003.
11. "Interconnect application note: Z-Pack HM-Zd PWB Footprint optimization for routing, AC & D Report, #20GC015–1, Rev. A, 2001.

© 2005 Wiley Periodicals, Inc.